



Experimental collisions of varying roughness wetted particles in the pendular regime compared to numerical simulations

Oscar J. Punch * and Daniel J. Holland †*Department of Chemical and Process Engineering, [University of Canterbury](https://www.canterbury.ac.nz), Christchurch 8041, New Zealand*Andreas Baumann  and Peter Eberhard *Institute of Engineering and Computational Mechanics, [University of Stuttgart](https://www.uni-stuttgart.de), Stuttgart 70569, Germany*

(Received 11 February 2024; accepted 6 May 2024; published 21 May 2024)

In this work rectilinear collisions of spheres coated in a thin viscous liquid film are considered, where the surface roughness of the spheres was varied. Experiments were performed using a Newton's cradle apparatus and the collision dynamics was measured using particle tracking velocimetry. The experiments showed that the dry and wet coefficient of restitution decreases as the roughness increases. Experimental collisions are compared with numerical simulations to examine criteria that limit the viscous force. We show that a model in which the liquid undergoes a glass transition is in excellent agreement with experimental measurements for smooth spheres, i.e., when the roughness of the spheres is less than the glass transition length. For rough particles, a constant minimum separation distance is more accurate than the glass transition model, which is consistent with the idea that contact occurs on the roughness elements. Furthermore, smoothed particle hydrodynamics (SPH) simulations were used to examine the viscous flow in detail. The SPH simulations accurately predicted the collision outcome for smooth spheres and showed that the maximum pressure was greater than the glass transition pressure used for the discrete element method simulations, supporting the feasibility of the glass transition model. The SPH simulations of rough particles indicate that during a collision the interstitial liquid flows through microchannels between roughness elements as a mechanism to alleviate pressure buildup, and reduce the viscous force consistent with the experimental observations.

DOI: [10.1103/PhysRevFluids.9.054302](https://doi.org/10.1103/PhysRevFluids.9.054302)

I. INTRODUCTION

Granular flows can be challenging to simulate due to irregular particle shape, size, and roughness [1,2], dissipative contact between particles [3], and nonlocal phenomena [4]. Recent studies have had success simulating dry granular flows using the discrete element method (DEM) [5,6]. However, many granular flows are not exclusively dry. The presence of small amounts of liquid in a granular flow has been found to greatly change the rheology of the flow [7,8]. Furthermore, agreement between DEM simulations and experiments of wet granular flows is poorer than for similar dry cases [9]. A possible limitation of wet granular flow studies is that they are not accounting for the surface roughness of particles correctly. This study examines the effect of surface roughness on the dynamics of wet particle collisions.

*Present address: Department of Chemical Engineering, Columbia University, New York, NY 10027, USA.

†daniel.holland@canterbury.ac.nz

When small amounts of liquid are present in a granular flow, the liquid forms bridges between particles; this is commonly referred to as the pendular regime [10]. As particles contact the liquid, they experience cohesive forces. These cohesive forces are comprised of capillary forces and viscous forces [11]. The capillary forces attract the particles to one another [12], while the displacement of the interstitial liquid generates a viscous force which slows the approaching particle [13]. The ratio of viscous forces to capillary forces, for contacting spherical particles, is given by a modified capillary number

$$\text{Ca} = \frac{3\mu v_{ij,0} r_{ij}}{\sigma h_{ij,0}}. \quad (1)$$

Here, μ is the viscosity of the interstitial liquid, $v_{ij,0}$ is the precollisional relative velocity, r_{ij} is the reduced radius, $r_{ij} = (r_1 r_2)/(r_1 + r_2)$, σ is the surface tension of the interstitial liquid, and $h_{ij,0}$ is the initial liquid film thickness. Capillary forces are considered negligible if $\text{Ca} > 3000$ [14].

Granular flows are typically comprised of small, rough, and inelastic materials [15]. Previous research has found particle roughness to affect many particle properties, such as the dry coefficient of restitution, Young's modulus, and Poisson ratio [16]. Further, when modeling dry granular flows it is common to account for surface roughness through the inclusion of a coefficient of friction term, and scaling laws have been proposed to account for the roughness [17]. A small change in the coefficient of friction often results in significant change in the macroscopic flow [18]. Yet, it is uncommon to account for particle roughness when modeling wet granular flows. Several studies assume that the particle-particle friction coefficient should be 0 when modeling wet granular flows as the surfaces of the particles do not contact due to the thin liquid layers [8]. On the other hand, a recent study showed that a small particle-particle coefficient of friction term was critical in describing postcollisional rotation for oblique collisions of smooth wetted particles [19].

It is challenging to investigate single-particle collisions within a larger macroscopic system due to the chaotic nature of the system. One previous study uses atomic force microscopy with a shear cell to measure the particle-particle forces [20]. However, due to the precise nature of the experiment, the results were affected by the interstitial liquid layer. Several groups have conducted studies using high-speed cameras to track collisions between a dry sphere and a wetted wall [21–24], a dry sphere and a wet sphere [14, 19, 25–28], or a sphere fully immersed in a liquid and a wall [29–32]. In these studies, the collisions are characterized using two dimensionless parameters: the Stokes number St , a ratio of inertial forces to viscous forces, and the coefficient of restitution e , a ratio of outgoing kinetic energy to incoming kinetic energy

$$\text{St} = \frac{m_{ij} v_{ij,0}}{6\pi \mu r_{ij}^2}, \quad (2)$$

$$e_{ij} = \frac{v_{ij,f}}{v_{ij,0}}. \quad (3)$$

Here, m_{ij} is the reduced mass of the particles $m_{ij} = (m_i m_j)/(m_i + m_j)$. These studies on binary collisions suggest that it is imperative that numerical models are able to accurately predict the outcome of a two-particle binary collision if they are to accurately model many-body macroscopic flows.

As two spheres approach each other, viscous forces arise from the displacement of the interstitial liquid [13]. The viscous forces decrease the relative velocity between the spheres. The spheres are slowed down until either some form of contact occurs, at which point the spheres' momentum starts to be reversed, and they begin to separate, or the viscous forces dissipate the momentum sufficiently such that the spheres remain agglomerated. Several authors have suggested that if the surfaces of the spheres are rough, less momentum is required for solid-solid contact to occur [25, 33]. It is proposed that this is due to contacting roughness elements protruding further through the liquid film. However, there has been no work conducted on how these roughness elements may influence collisions between two particles, or affect the flow of the liquid as it is displaced. Previous work has been conducted on smooth particles contacting a roughened planar plate and found that roughness

affects the coefficient of restitution; however, the trends are not consistent. One study found that as the plate roughness is increased, particles rebound from the plate with more momentum [34], while another study finds that they rebound with less momentum depending on the Stokes number [35].

For numerical simulations of wet particles, the viscous force is derived from a modified version of Reynolds lubrication theory [36]. The viscous force is a function of thickness of the interstitial liquid between the particles. Thus, as the separation between particles tends towards zero, the viscous force tends towards infinity. The viscous force can reach unrealistically large values if the separation distance is allowed to reach very small values. For numerical models of wet granular flows, it is common to implement some minimum separation distance to ensure numerical stability [37,38]. However, it is not clear how the collision should proceed when the separation distance reaches the minimum separation; one model allows for the collision to continue but uses the minimum separation distance to calculate the viscous force [39], while another model instantly reverses the particle momentum when this minimum separation distance is reached [33].

The implementation of the minimum separation distance for numerical simulations is also not trivial. Most studies suggest that the minimum separation distance should be equal to the surface roughness of the spheres [37]. However, often this minimum separation distance is orders of magnitude greater than the real surface roughness of the particles. Typical granular materials have roughness $\approx 100 \mu\text{m}$ [40]. Yet, most studies use smooth particles which have a roughness $\leq 1 \mu\text{m}$. Despite this, the minimum separation distance employed in numerical simulations is on the order of $10 \mu\text{m}$ [37], i.e., much greater than the roughness. One study proposes the idea that at very small separation distances, the liquid increases in viscosity, due to a pressure dependence [41]. This increase in viscosity may cause the interstitial liquid to undergo a glass transition and initiate a solidlike contact between the particles [42]. Recent studies have found significantly better agreement between binary rectilinear collision experiments and numerical models which use a minimum separation derived from the glass transition theory [27,33]. However, electrical conductivity measurements recently showed that the surface of particles does contact each other during a wet collision [28]. Hence, there is still significant confusion around the dynamics of wet particle collisions and the validity of the glass transition model.

To investigate the validity of the glass transition model there must be direct comparison with experimental measurements of collisions of smooth and significant roughness wet spheres. One particular study [30] provides significant experimental measurements of fully immersed rough spheres contacting a smooth wall. However, it is challenging to use the experiments in this study to investigate the validity of the glass transition model as the viscosity used in the work is very low and so the length scale associated with a glass transition is very small and exceeded by the roughness for all cases. Thus, there is a need for more rough wet particle experiments and specifically those for which at low relative velocity the roughness should dominate the collision dynamics and for high relative velocity, the glass transition should dominate the collision dynamics.

Another numerical technique sometimes used to model liquid-solid interaction is smoothed particle hydrodynamics (SPH). SPH is a mesh-free Lagrangian method which solves the Navier-Stokes equations at discrete integral points over the domain [43,44]. An advantage of SPH over traditional mesh-based computational fluid dynamics (CFD) methods is that there is no remeshing required for a deforming domain. For traditional CFD methods, remeshing can be extremely computationally expensive if the boundary is continuously deforming around a complex body. Recently, SPH has had success modeling fluid flow around complex geometries [45]. Furthermore, SPH is most suitable for modeling liquid-solid interaction when the solid body is rigid [46], which is common for wet granular flows. Some SPH studies simulating wet granular flows have found good agreement with experimental results [47]; however, these studies are uncommon due to the computational cost of SPH.

Here, the rectilinear collisions of two smooth or rough spheres coated in thin viscous films are studied. The collisions are conducted using a traditional Newton's cradle apparatus, but where the stationary particle is dipped in viscous silicone oil prior to contact. The effect of particle roughness on the collision dynamics is considered by comparing measurements of smooth spheres and spheres

with an induced surface roughness between 14 and 57 μm . The Stokes number for the collisions is between $0 < \text{St} < 16$. The experimental results are compared to numerical simulations using the discrete element method with a viscous force model that uses either a minimum separation distance derived from the glass transition pressure of the interstitial liquid, or a constant minimum separation distance based on the surface roughness of the particles. Finally, select collisions are also simulated using smoothed particle hydrodynamics to investigate the flow of interstitial liquid during a collision.

II. THEORY

An overview of the theory used to describe a rectilinear collision of wetted spherical particles is provided here. Further, the implementation of this theory into a DEM framework is given. The Navier-Stokes equations and their implementation into an SPH framework are also provided.

A. Discrete element modeling

DEM is used to numerically model particle motion. Here, a soft-sphere implementation using LIGGGHTSTM was used [48]. For a rectilinear collision, tangential forces are negligible and, hence, the translational motion of a dry particle i contacting a wet particle j , is described by

$$m_i \frac{d\mathbf{v}_i}{dt} = \sum_j (F_{ij}^n + F_{\text{cap},ij}^n + F_{\text{visc},ij}^n), \quad (4)$$

where \mathbf{v}_i is the translational velocity of the i th particle. We now drop the superscript n for clarity, as all forces act in the normal direction. The forces during a collision are represented by the solid contact force F_{ij} , capillary force $F_{\text{cap},ij}$, and the viscous force $F_{\text{visc},ij}$. Here, $F_{\text{cap},ij}$ is considered negligible due to a high value of Ca . A solid-solid contact model is used in DEM when the solid surfaces intersect. For this study we use the normal component of the Hertz-Mindlin contact model which is

$$F_{ij} = k\delta_{ij} - \gamma v_{ij}. \quad (5)$$

Here, k is the elastic constant, δ is the overlap distance of two particles, and γ is the viscoelastic damping. Further description of the Hertz-Mindlin model is available in the LIGGGHTSTM documentation [48].

B. Viscous force modeling

A schematic of a collinear collision of two spheres, where the stationary sphere is coated in a thin viscous film, is given in Fig. 1. The separation distance between the spheres h_{ij} is defined as the distance between the centroids of the two spheres (x_i and x_j), minus the radii of each sphere, i.e., $h_{ij} = x_j - x_i - (r_i + r_j)$. When the striking sphere first contacts the liquid film of the stationary sphere, we have $h_{ij} = \delta_j$ and this is referred to as $h_{ij,0}$.

The viscous force model for two approaching spheres is derived from Reynolds lubrication theory [36]. Here, we consider a viscous force model proposed in [12] which includes the curvature of the spheres and the deformation of the interstitial liquid during the collision. The viscous force is given by

$$F_{\text{visc}} = \frac{6\pi\mu r_{ij}^2 v_{ij}}{h_{ij}} \left(1 - \frac{h_{ij}}{2h_{ij,0} - h_{ij}}\right)^2. \quad (6)$$

Here, $h_{ij,0}$ is the sum of the film thickness on both spheres at $t = 0$ s.

Numerical viscous force models require the implementation of a minimum separation distance to ensure numerical stability. This minimum separation distance is referred to as h_{min} . It was first proposed in [49] that there must be some governing rebound criteria which can describe whether a

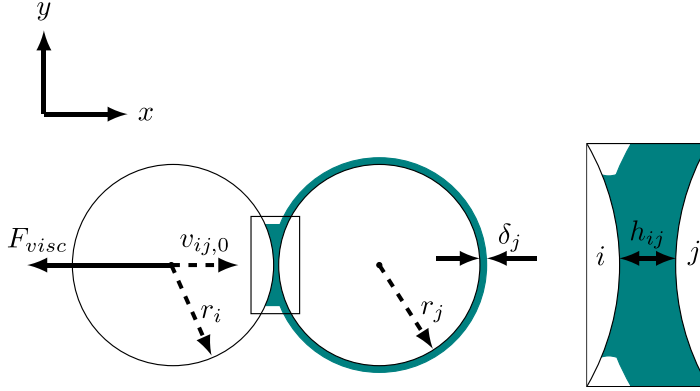


FIG. 1. Schematic of a collinear collision between dry striking particle i and wetted stationary particle j .

sphere will rebound from a given surface which has been wetted with a thin layer of viscous fluid. Here we consider two forms of h_{\min} : a constant h_{\min} which is given by the roughness of the spheres and $h_{\min} = h_{\text{Ra}} \approx \text{Ra}$, where Ra is the average roughness of a sphere, or h_{\min} which is based on the glass transition pressure of the interstitial liquid and is given by

$$h_{\min} = h_{\text{gt}} = \sqrt{\frac{3\mu r_{ij} v_{ij}}{P_{\text{gt}}}}, \quad (7)$$

where P_{gt} is the glass transition pressure of the interstitial liquid. It is assumed that if $h_{\text{Ra}} > h_{\text{gt}}$, the surface roughness will be the dominant contact mechanism and the collision should not be able to be described by Eq. (7). To approximate the hard-sphere collision in [12,49], the viscous force is set to 0 when $h_{\min} > h_{ij}$. This method has seen success in previous studies [19,27].

C. Smoothed particle hydrodynamic modeling

Smoothed particle hydrodynamics (SPH) is a numerical modeling technique to model continuum media as a set of discretization points called particles [43,44]. Using these particles, SPH solves the Navier-Stokes (NS) equations to resolve fluid flow. Unlike traditional computational fluid dynamics (CFD) methods (e.g., the finite-volume method), where the domain is discretized into a mesh, SPH is an entirely mesh-free Lagrangian method. This makes it advantageous in a problem like the collision of two spheres with an interstitial liquid, as the domain is constantly evolving, which may be computationally expensive to track using traditional CFD methods.

Two approximations are made for SPH: the *kernel approximation* to represent a function and its derivatives in an integral form, and the *particle approximation*, which describes the discretization using moving points [50,51]. First, we introduce an identity

$$A(\mathbf{x}) = \int_{\mathbf{x}' \in \Omega} A(\mathbf{x}') \delta(\mathbf{x} - \mathbf{x}') d\Omega, \quad (8)$$

where $A(\mathbf{x})$ is a function which needs to be approximated, \mathbf{x} is a position in space, and Ω is the complete domain. The Dirac delta distribution is applied

$$\delta(\mathbf{x} - \mathbf{x}') = \begin{cases} \infty, & \text{for } \mathbf{x} = \mathbf{x}' \\ 0, & \text{else.} \end{cases} \quad (9)$$

Delta distributions $\delta(\mathbf{x} - \mathbf{x}')$ are replaced by a kernel function (or smoothing function) $W(\mathbf{x} - \mathbf{x}', h)$, where h is the smoothing length. We then get

$$A(\mathbf{x}) \approx \langle A(\mathbf{x}) \rangle = \int A(\mathbf{x}')W(\mathbf{x} - \mathbf{x}', h)d\Omega. \quad (10)$$

The kernel $W(\mathbf{x} - \mathbf{x}', h)$ can be selected by the user, but must obey the unity condition, Dirac property, and the compact support condition [52]. For the approximation of the continuum, the integral is replaced with the weighted sum of the contributions at discrete points, the so-called particles, leading to the particle approximation

$$\langle A(\mathbf{x}) \rangle = \sum_b \frac{m_b}{\rho_b} A_b W(\mathbf{x} - \mathbf{x}_b, h). \quad (11)$$

Instead of considering all particles in the domain, the sum runs only over the neighboring particles b as the kernel function W vanishes for most particle pairings due to its compact support. Further, m is the particle's mass, and ρ is the density at the particle position. The term $\frac{m_b}{\rho_b} = d\Omega_b$ corresponds to a certain volume assigned to a particle b . In general, SPH can be applied to approximate arbitrary partial differential equations. Here we want to solve the fluid flow domain. To do this, we must introduce the Navier-Stokes equation, continuity equation, kinematics equation, and the equation of state.

The Navier-Stokes equations are the basis for all flows and they are extremely general. The NS equations are derived from the balance of linear momentum for an infinitesimal volume element with many different forces considered. They read as follows:

$$\rho \frac{d\mathbf{v}}{dt} = \rho \left(\frac{\partial \mathbf{v}}{\partial t} + (\mathbf{v} \cdot \nabla) \mathbf{v} \right) = \rho \mathbf{g} - \nabla P + \mu \nabla^2 \mathbf{v}, \quad (12)$$

where \mathbf{v} is velocity, t is time, \mathbf{g} is gravity, and P is pressure [53]. The NS equations are complemented by the continuity equation

$$\frac{d\rho}{dt} = -\rho \operatorname{div} \mathbf{v}, \quad (13)$$

and the relation between position \mathbf{n} and velocity \mathbf{v} from a kinematics equation

$$\frac{d\mathbf{n}}{dt} = \mathbf{v}. \quad (14)$$

Here, \mathbf{n} is a position with coordinates in (x, y, z) . Finally, the equation of state is needed to ensure that we have the same number of equations and unknowns, eight equations for $\rho, \mathbf{v}, P, \mathbf{n}$. For SPH, the Tait equation is commonly used as the equation of state [54], relating density and particle pressure; this is given by

$$P = \frac{C_0^2 \rho_o}{\zeta} \left[\left(\frac{\rho}{\rho_o} \right)^\zeta - 1 \right], \quad (15)$$

where C_0 is the speed of sound, ρ_o is a reference density, and ζ is the polytropic index. This equation of state is quite stiff, requiring small step sizes during the numerical integration. Therefore, an artificial fluid with a lower speed of sound is usually used instead of the modeled fluid's physical properties. Thereby, small density fluctuations of around 1% are allowed by choosing the speed of sound as 10 times the maximum fluid velocity [55]. This approach is commonly referred to as weakly compressible SPH formulation.

For SPH, Eqs. (12) and (13) need to be solved at discrete particle positions. Thus, the equations must be altered for the SPH environment. To improve the readability, the kernel function $W(\mathbf{x}_a - \mathbf{x}_b, h)$ is abbreviated in the following as W_{ab} and ∇_a refers to the partial derivative with

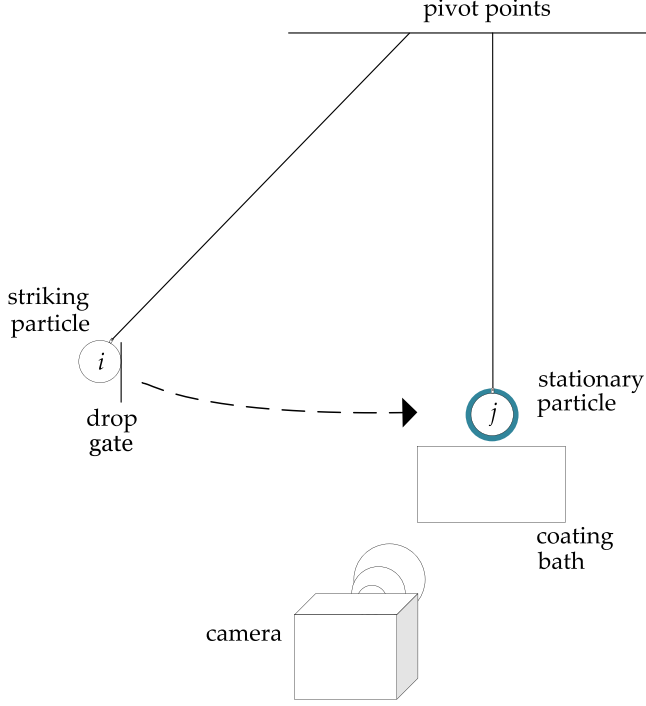


FIG. 2. Schematic of the Newton's cradle setup.

respect to the position evaluated at particle a . The equations are as follows: the NS equation in SPH form is

$$\begin{aligned} \frac{d\mathbf{v}}{dt} \Big|_a = & \mathbf{g} - \sum_b m_b \left[\left(\frac{P_a}{\rho_a^2} + \frac{P_b}{\rho_b^2} \right) \right. \\ & \left. - \frac{1}{\rho_a \rho_b} \frac{(\mu_a + \mu_b) \mathbf{v}_{ab} \cdot \mathbf{n}_{ab}}{|\mathbf{n}_{ab}|^2 + 0.01h^2} \right] \nabla_a W_{ab}, \end{aligned} \quad (16)$$

and the continuity equation in SPH form

$$\frac{d\rho}{dt} \Big|_a = \rho_a \sum_b \frac{m_b}{\rho_b} (\mathbf{v}_a - \mathbf{v}_b) \cdot \nabla_a W_{ab}. \quad (17)$$

Further details about the SPH method are provided in the literature [50,51].

III. METHODS

A. Newton's cradle setup

Here we use a Newton's cradle setup to investigate the particle contact dynamics. This apparatus has been used successfully in several previous studies for wet particle contact dynamics [14,19,27,28]. Figure 2 shows a schematic of the setup. In this modified apparatus, the strings suspending the particles are sufficiently long such that during the imaged time frame it can be assumed the usual restoring force associated with a pendulum is negligible. Thus, only translational motion in the x direction is considered. Here, we use a string length of 1 m. For a given collision, all particles are made of the same material and the spheres are 1 in in diameter, prior to inducing

a roughness. The material of the particles is either 316 stainless steel, AISI 52100 chrome-plated carbon steel, or alumina.

Prior to collision, the dry suspended particle is dipped in silicone oil; the striking particle is not coated in oil. The metal particles are dipped in silicone oil with a viscosity of $\mu = 3$ Pa s and the alumina particles are dipped in silicone oil with a viscosity of $\mu = 1$ Pa s. For these viscosities, the range of Stokes numbers investigated in this study are $0 < St < 16$, which is similar to those measured in wet spouted beds [56]. After removing the suspended particle from the oil, the oil is allowed to drain for a predetermined period of time. This period of time is 180 s for the metal spheres, and 120 s for the alumina spheres. The striking particle is then released from the drop gate and contacts the stationary particle. The particles are imaged at 5000 frames per second using a Photron SA-5 camera with a 75-mm lens at 1024×1024 resolution and the Photron Fast Viewer 4 software. The setup requires an LED backlight to image at such high frame rate which produces high-contrast images improving particle tracking.

The particle position is tracked in GOM Correlate® through the suspension hole at the top of the particles. The contrast between the white back light shining through the hole, and the silhouetted edge of the hole allows for accurate positional tracking. Particle position is exported from GOM and the velocities are resolved using MATLAB. The position of the particles at any instance in time can only be resolved to ~ 50 μm accuracy due to the resolution of the camera. To resolve this positional inaccuracy, a Holoborodko smoothing differentiator [57] with a filter length of 5 is used to determine the current velocity of the particles, from the two previous positional measurements and the two future positional measurements. This smoothing differentiator is given by

$$v_i = \frac{2(x_{i+1} - x_{i-1}) + x_{i+2} - x_{i-2}}{8\Delta t}, \quad (18)$$

where v_i is the current velocity of the particle in the x direction, x_i is the position of the particle at time step i , and Δt is the time step between frames. The velocities of the particles are then used to determine the Stokes number and the wet coefficient of restitution. Images where the particles are rotating postcollision were discarded. The Stokes number is calculated from the relative velocity between the stationary particle and the striking particle prior to contact; this is averaged over at least 50 time steps prior to collision. Thus, the error associated with St is low, and is in the range of 3.5%–5%.

B. Particle surface roughness characterization

It is hypothesized that if the particle roughness is greater than the minimum separation distance associated with the glass transition, then the particle roughness will be the minimum separation distance [12,33]. Figure 3 shows how h_{gt} changes as a function of St . From Fig. 3 we can ascertain that for the roughness to dominate the collisions, the particle roughness should be greater than 15 μm for the chrome steel spheres and 5 μm for the alumina spheres. In this study we also consider stainless steel spheres, which differ from h_{gt} for the chrome steel spheres by approximately 2.5%.

To apply the microspheres to the metal particles, a thin layer of cyanoacrylate glue was applied to the entire surface of the metal particles and they were dunked in a crucible filled with the glass microspheres. The metal spheres were sandblasted using mesh 30–60 garnet prior to application of the glue and microspheres. It was found that the dry coefficient of restitution decreased for the metal particles after applying the microspheres. It was considered that this may be due to some inelasticity caused by the thin glue layer, however, previous authors have also reported a decrease in dry coefficient of restitution due to increased surface roughness [35,58]. A different approach was taken with the alumina spheres to ensure there was no interference from the cyanoacrylate glue on the dry coefficient of restitution. Instead, the alumina spheres were sintered with an alumina bonding coating to adhere the powder. The alumina spheres could not be sandblasted prior to sintering of the alumina powder due to the hardness of alumina. Instead, the ceramic spheres were thermally etched using the following procedure: ramped up at 15 °C/min until 1300 °C, and kept at 1300 °C for

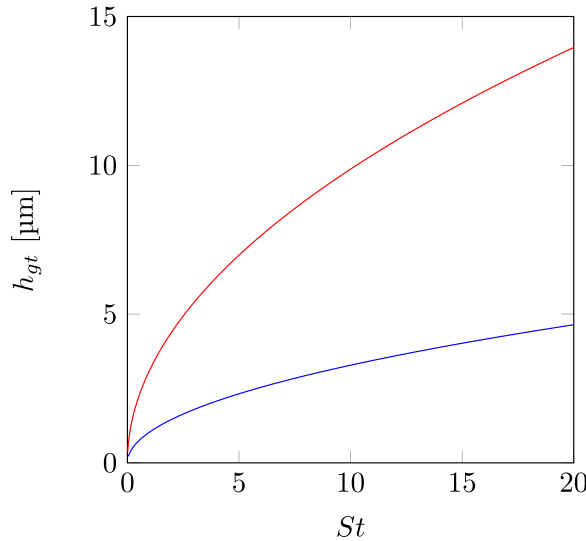


FIG. 3. The glass transition pressure associated length scale as a function of St for chrome steel spheres (—) and alumina spheres (—). The chrome steel case uses $\mu = 3$ Pa s while the alumina case uses $\mu = 1$ Pa s, as these viscosities correspond to the viscosity used in the collision experiments. The maximum velocities correspond to a value of $St = 20$, as that is the maximum achievable experimentally. The glass transition pressure corresponds to $P_{gt} = 4 \times 10^8$ Pa.

25 min in flowing air (100 mL/min). The system was then cooled down at $15^\circ\text{C}/\text{min}$. The thermal etching was conducted using a Mettler TG1 Thermobalance. The alumina spheres were then coated in a thin layer of Resbond 989 and dipped into the alumina powder to adhere the alumina powder. The spheres were then placed in the aforementioned oven with a $2^\circ\text{C}/\text{min}$ ramp until 90°C for which they were kept for 2 h. The temperature of the oven was then ramped up by $2^\circ\text{C}/\text{min}$ to 120°C , for which the spheres were kept for 1 h. Finally, the oven temperature was increased by $2^\circ\text{C}/\text{min}$ until 250°C , which was held for 1 h.

In all cases, the surface roughness of the overall particle was taken to be equivalent to the median radius of the applied microspheres and powder. The microspheres and powder were chosen such that the difference in particle radius was significant and, therefore, the difference in induced roughness would be significant. The microsphere-powder median diameter was measured using laser diffraction spectrometry using the Mie method [59]. Figure 4 shows the particle size distribution of the samples. All samples except the median diameter $28.6\text{-}\mu\text{m}$ sample have some peak volume percent of 15%–17%. This high-volume percentage indicates that the spread of particle diameters is tight and sieving would likely have negligible effect. The sample with median diameter $28.6\text{ }\mu\text{m}$ was sieved using a sieve shaker stacked with 63-, 45-, and $38\text{-}\mu\text{m}$ sieves, but it was found to have insignificant effect (only postsieved results are presented in Fig. 4). The median radius of the samples presented in Fig. 4 are greater than all values of h_{gt} presented in Fig. 3, except for the median radius $14\text{-}\mu\text{m}$ sample which is slightly less than h_{gt} for chrome steel spheres at the highest St .

Detailed images of the surface of the particles were obtained through scanning electron microscopy (SEM) using the backscattered-electron detection method (BED). The spheres were imaged under low vacuum conditions (70 Pa). The images obtained from SEM imaging of the surface of the spheres are shown in Fig. 5 for both the smooth and rough spheres. Only stainless steel spheres and alumina spheres were imaged. Chrome steel particles have been assumed to have the same topography as the stainless steel particles. The surfaces of all the spheres are quite different. There are a wider range of particle sizes in Fig. 5(c) than in Figs. 5(d)–5(f) which is in agreement

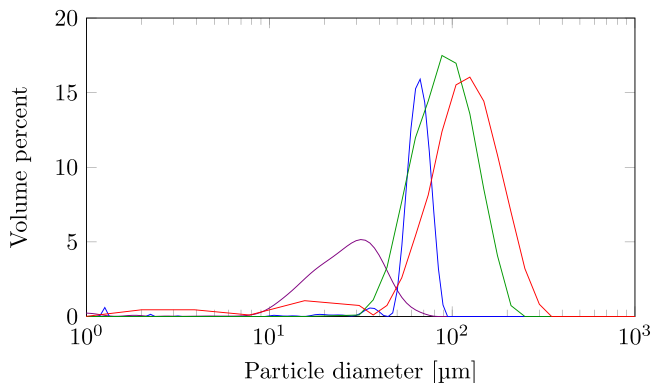


FIG. 4. Volume percent of the microspheres and powders applied to the spheres. The median diameters for the microspheres are 28.6 μm (—) and 65.6 μm (—), while the median diameters for the powders are 87 μm (—) and 114 μm (—).

with the particle size distribution shown in Fig. 4. There are also fibers present in Fig. 5(c) which are not part of the microspheres. The origin and makeup of these fibers is unknown, but it is likely they are dust particles collected during the sieving process. The amount of void space on the surface of the particles was not quantitatively measured. However, it can be seen that the void space is minimal. The surfaces of particles shown in Fig. 5 appear to be uniform and closely resemble monolayer coverage. Thus, we can say that the surface of the particles has an induced roughness characterized by the median radius of the applied microspheres and powders. From here on, we will refer to the roughness of the spheres by the median radius of the microspheres and powders.

An additional set of roughened particles were obtained by sandblasting smooth stainless steel particles with garnet of mesh size 30–60. The surface roughness induced by the sandblasting was estimated using measurement of a tip-based profilometer on a stainless steel plate which had undergone the same sandblasting treatment. The measurement of the surface of the stainless steel plate indicated that the height of surface deviates up to 10 μm in some areas. Thus, here it is assumed that the roughness of the sandblasted spheres is $R_a \approx 10 \mu\text{m}$.

C. Film thickness measurement

The thickness of the silicone oil film coating the suspended particles must be determined to ensure that the collision is correctly characterized and reproducible. To determine the oil film thickness, a single particle was dipped in silicone oil ($\mu = 1 \text{ Pa s}$ for the alumina spheres, and $\mu = 3 \text{ Pa s}$ for the steel spheres) and imaged at 3-s intervals. A 10.2-megapixel Nikon D80 camera with a 135-mm zoom lens was used to image the stainless steel and chrome steel particles while a 62.0-megapixel Sony $\alpha 7RIV$ camera with a 135-mm zoom lens was used to image the alumina particles. An example snapshot is shown in Fig. 6. The images are analyzed in MATLAB. The images are binarized using the inbuilt function *imbinarize*. The binarization threshold is set such that the edge of the particle is well defined. The widely known Otsu threshold selection method [60] was used to ensure that the particle edge was well defined. Once the images are in their binarized form, the particle centroid is located using the inbuilt function *bwdist*. The function *bwdist* calculates the Euclidean distance separation of a white pixel from a black pixel in a given binarized image. For a circle, like in our system, this function has a maximum at the centroid, and is analogous to the radius of the particle plus the thickness of the oil coating. The known particle radius can then be subtracted from this maximum, to return the thickness of the oil film. This method has been used successfully in previous studies [14,19,27].

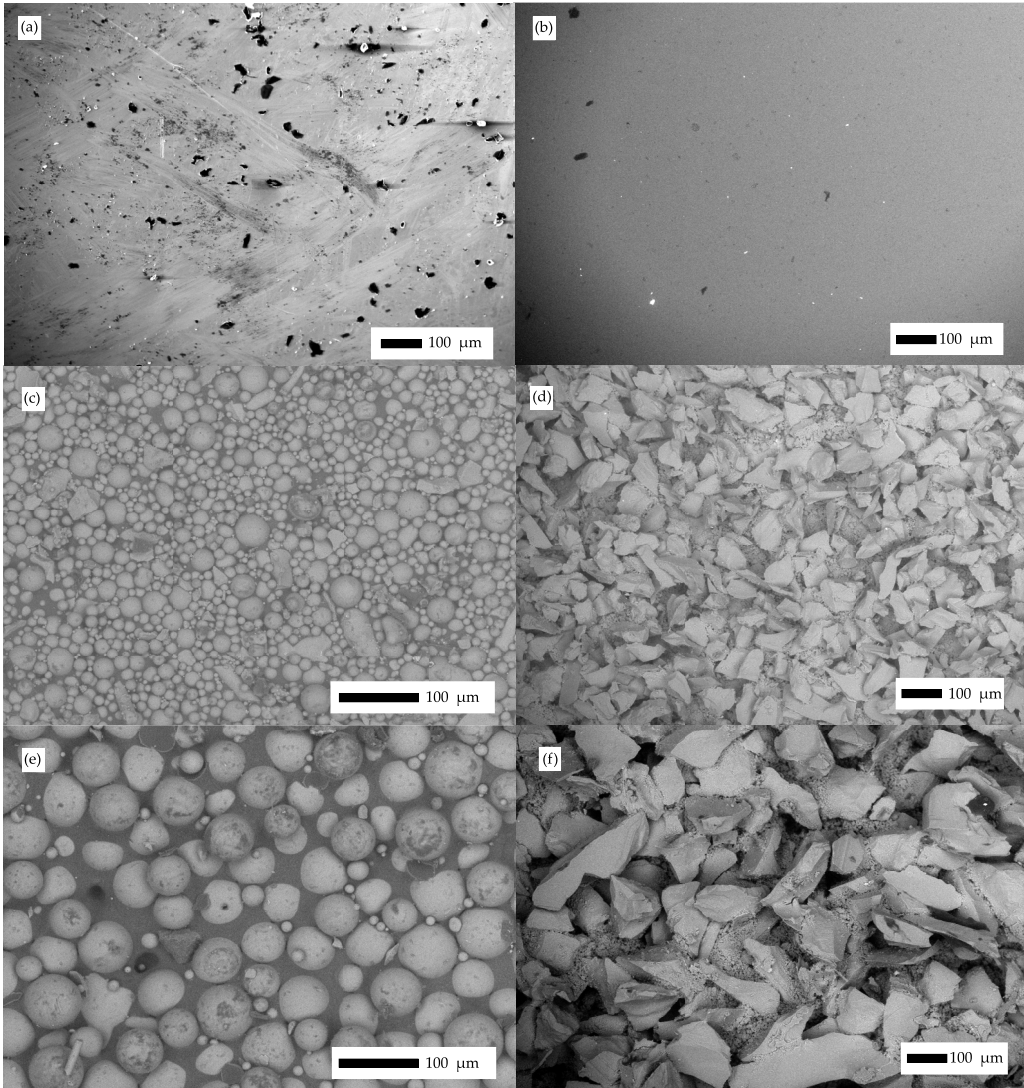


FIG. 5. SEM images via backscatter electron detection for stainless steel (left) and alumina particles (right). (a), (b) The smooth spheres ($R_a < 1 \mu\text{m}$) for this study, while (c)–(f) are the rough sphere surfaces. The roughness for the rough cases are (c) $14 \mu\text{m}$, (d) $32.5 \mu\text{m}$, (e) $44 \mu\text{m}$, and (f) $57 \mu\text{m}$.

For the roughened metal particle case, the interface where the oil layer begins is dependent on the diameter of the spherical roughness elements on the particle. It is unlikely that two colliding particles will collide such that the vertex of the roughness elements on the striking particle contact the vertex of the roughness elements on the stationary particle. Thus, if the oil thickness is taken as everything other than the radius of the particle and the diameter of the applied microspheres and powder, it will be underestimated. The position where the roughness elements contact could occur, r , is bound, $0 \leq r \leq R_m$, where R_m is the median radius of the microspheres and powders. In this study, the oil layer has been chosen to begin at the average height of collision of two colliding microspheres \bar{H} . Thus, the true radius of the particle R_T is taken as $R_T = R + R_m + \bar{H}$. The average



FIG. 6. Example snapshot of an alumina smooth particle coated in 1 Pa s silicone oil. The dripping process is exclusively gravity driven.

height of the microspheres is taken from the average height of a hemisphere and given by

$$\bar{H} = \frac{1}{\pi R_m^2} \int_0^{R_m} (R_m^2 - r^2)^{1/2} 2\pi r dr. \quad (19)$$

Equation (19) elegantly reduces to $\bar{H} = 2R_m/3$. It should be noted that there has been no attempt to quantify the thickness of the cyanoacrylate glue layer and it has been assumed to be negligibly thin. For the alumina particles, this method was not used as the roughness elements are larger and aspherical. Instead, the diameter of the sphere was precisely measured by imaging the dry sphere and resolving the diameter through a pixel to mm conversion. This measurement was verified using a micrometer and the two values were found to be within ± 0.01 mm of each other.

Previous studies have concluded that the collision outcome is strongly dependent on the oil film thickness [14,33]. It is important to ensure that the oil film thickness is consistent throughout all experiments so that any differences in collision outcome cannot be attributed to a difference in oil film thickness. Figure 7 shows the thickness of the oil film over time. For the metal sphere collisions we use a drip time of 180 s, and for the alumina collisions we use a drip time of 120 s. At these drip

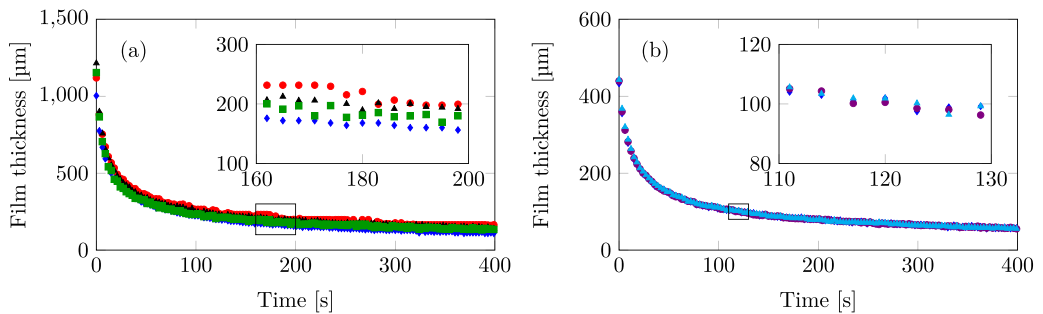


FIG. 7. Oil film thickness over time for (a) stainless steel and (b) alumina particles. The markers correspond to different roughness particles: smooth (\blacklozenge), sandblasted (\blacksquare), 14 μm (\bullet), 32.5 μm (\blacktriangle), 44 μm (\blacklozenge), and 57 μm (\blacktriangle).

TABLE I. Material properties of the particles and liquid used in the DEM simulations.

	Symbol	Stainless steel	Chrome steel	Alumina	Unit
Radius	r	12.7	12.7	12.7	mm
Density	ρ_s	7960	7800	3900	kg m^{-3}
Young's modulus	E	200	200	380	GPa
Poisson ratio	ν	0.265	0.27	0.22	
Smooth dry coefficient of restitution	e_{dry}	0.90	0.95	0.99	
Sandblasted dry coefficient of restitution	e_{dry}	0.82			
14- μm rough dry coefficient of restitution	e_{dry}	0.72	0.66		
32.5- μm rough dry coefficient of restitution	e_{dry}	0.65	0.53		
44- μm rough dry coefficient of restitution	e_{dry}			0.22	
57- μm rough dry coefficient of restitution	e_{dry}			0.22	
Viscosity	μ	3	3	1	Pa s

times, the further change in film thickness is minimal and the oil film thickness was reproducible for each experiment. From Fig. 7 it can be seen that the oil film thickness at 180 s for the smooth, sandblasted, 14- and 32.5- μm cases are 168, 181, 200, and 220 μm , respectively. If the additional thicknesses of the microspheres are ignored the oil film thickness at 180 s for the 14- and 32.5- μm cases are 230 and 275 μm , respectively. The metal sphere results presented in Fig. 7 are for stainless steel spheres; it is assumed that the film thickness on the chrome steel spheres is equal to that for stainless steel spheres. The film thickness for the alumina spheres was measured to be $h_{ij,0} = 100$ μm at 120 s, regardless of roughness.

D. DEM and SPH simulation setup

DEM simulations are conducted using the open-source framework LIGGGHTSTM. The DEM simulation parameter values are shown in Table I. Here we use a half-time-step velocity Verlet scheme to integrate Eq. (4) with a time step of 1×10^{-8} s [61]. The particle position, velocity, and force data in the x , y , and z directions are output every 1000 time steps. The simulations were run for a maximum run time of 0.2 s. This value of 0.2 s was chosen as it was the time prior to gravity forces significantly slowing the spheres due to the pendulum motion for the experiments. The spheres are considered separated if $F_x = 0$. The postcollisional velocities of the particles are taken as the first instance where $F_x = 0$. If F_x does not reach zero during a simulation, the particles are considered agglomerated and the coefficient of restitution is resolved using the velocities from the final time step ($t = 0.2$ s).

The SPH simulations are conducted using the software framework PASIMODO [62], developed at the Institute of Engineering and Computational Mechanics at the University of Stuttgart. The SPH simulations are set up to mimic a single smooth stainless steel sphere collision at an initial striking velocity of $v_{ij,0} = 0.205$ m s^{-1} ($St = 3$) and a coefficient of restitution of $e = 0.41$. The simulation parameters are shown in Table II.

A snapshot, prior to collision, of the simulation setup is shown in Fig. 8. The simulation consists of three parts: the solid DEM spheres, the liquid SPH particles, and the SPH boundary particles. The solid DEM spheres have the same material properties as the stainless steel spheres used in the experiments. The liquid SPH particles are used to model the viscous silicone oil film that coats the spheres. The SPH boundary particles model a nonslip boundary condition [63] in the interaction with the liquid SPH particles. The SPH boundary particles impose all forces acting on them onto the DEM spheres. However, the mass and inertia of the SPH boundary particles are not considered for the DEM spheres. It would be computationally expensive to model the entire sphere coated in a thin viscous film using SPH. Thus, here we only consider the region where the pressure in fluid is

TABLE II. SPH simulation parameters.

Property	Symbol	Value	Unit
Sphere radius	r	12.7	mm
Sphere density	ρ_s	7960	kg m^{-3}
Young's modulus	E	2e11	Pa
Poisson ratio	ν	0.35	
Initial striking velocity	$v_{ij,0}$	0.205	m s^{-1}
Dry coefficient of restitution, smooth	e_{dry}	0.90	
Roughness size	r_m	32.5	μm
Roughness distance	$3 \times r_m$	97.5	μm
Fluid density	ρ_f	970	kg m^{-3}
Fluid viscosity	μ	3.0	Pa s
Film thickness	$h_{ij,0}$	168	μ

expected to be $P > 0$ at some instance during the collision. This region of interest was calculated from [12] and has a 2-mm radius.

For the interaction of the two solid DEM spheres, the Hertzian-based Kuwabara-Kono contact model was applied [64]. The contact stiffness is calculated from Young's modulus, and a dissipation constant is fitted from dry simulations to match the coefficient of restitution to the dry experimentally measured coefficient of restitution ($e_{\text{dry}} = 0.90$, in case of smooth spheres, and $e_{\text{dry}} = 0.65$ for the rough spheres). Interaction between the surfaces of the two DEM spheres only occurs when all the liquid is displaced from the contact zone and the spheres come directly in contact.

For boundary and liquid SPH particles, a kernel gradient correction [65] is applied to enforce the exact interpolation of linear gradients in areas where the kernel support is not filled, e.g., at the domain borders. The stiff behavior of the equation of state used to evaluate the pressure causes spurious density and pressure fluctuations leading to inaccurate flow field prediction. Therefore, an additional density correction is applied by adding a diffusion term to the momentum equation. This approach is called δ -SPH and was first proposed in [66].

For the simulation of rough spheres, solid 65- μm ($r_m = 32.5 \mu\text{m}$) DEM spheres are embedded within the larger DEM spheres to act as roughness elements. The centroid of the 65- μm spheres is placed on the surface of the larger DEM sphere to form a hemispherical roughness element. The 65- μm spheres are arranged in a square grid pattern and spheres are separated by a distance of $3 \times r_m$ to allow fluid flow through the roughness element channels. The liquid is placed on the surface of

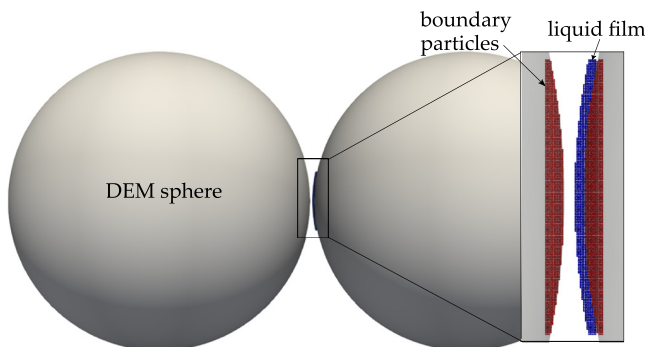


FIG. 8. Snapshot depicting the different domains during an SPH simulation of a smooth dry sphere striking a wetted sphere.

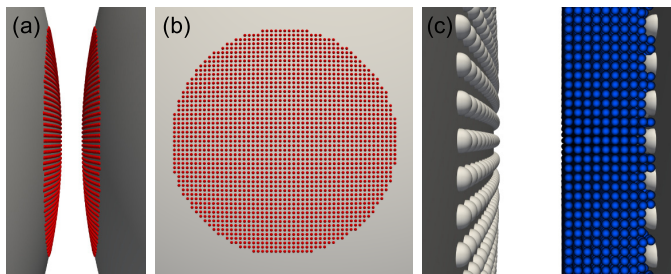


FIG. 9. Snapshot depicting the roughness elements and liquid for a rough SPH simulation: (a) side view with the roughness spheres colored red for an increased contrast, without the fluid displayed, (b) frontal view onto one of the spheres, and (c) view onto the fluid phase, cut in the collision plane, colored blue.

larger DEM spheres such that the roughness elements are fully submerged in the liquid prior to collision. Figure 9 shows an example of the described rough sphere used.

IV. RESULTS

A. Dry coefficient of restitution

The dry coefficient of restitution e_{dry} was measured by contacting a single stationary dry particle with a dry striking particle. Experiments were repeated for a range of velocities for the three material cases, SS, CS, and alumina, and the corresponding roughnesses ($<1 \mu\text{m}$, $14 \mu\text{m}$, and $32.5 \mu\text{m}$ for the SS and CS spheres, and $<1 \mu\text{m}$, $44 \mu\text{m}$, and $57 \mu\text{m}$ for the alumina spheres). An additional set of sandblasted stainless steel spheres ($R_a \approx 10 \mu\text{m}$) was also measured. It is important to correctly define e_{dry} as any changes in e_{dry} will also affect the wet coefficient of restitution e . Figure 10 shows the effect of increasing initial velocity on e_{dry} . The results shown in Figs. 10(a)–10(c) indicate that e_{dry} is constant over the range of investigated velocities. It has been stated that the dry coefficient of restitution is inversely proportional to the striking velocity [67]. However, this inversely proportional relationship is only observed for a high range of velocities ($>3 \text{ m s}^{-1}$) and can thus be considered negligible here. The dry coefficient of restitution for each particle was determined from the mean of the measurements of e_{dry} across all striking velocities which is shown in Fig. 10(d). The error was taken as the standard deviation across each data set. From Fig. 10(d) it is seen that as the particle roughness increases, e_{dry} decreases. The difference in e_{dry} across particle roughness is attributed to the change in particle roughness. Previous studies have found that as particle roughness increases, the normal dry coefficient of restitution decreases due to asymmetric force distribution during contact due to contacting roughness elements [35,58]. The difference in e_{dry} between the smooth spheres and the roughened spheres for all materials is significant. It is particularly significant for the alumina spheres, presumably due to the larger variation in size and shape of the alumina micropowder.

B. Experimental collision of rough wet spheres

Here, we consider collisions between a dry striking sphere and a stationary wetted sphere. The spheres are contacted by a dry sphere of the same roughness and material type. Figure 11 shows the effect of particle roughness on e for a range of St. All roughness cases have some critical St; when exceeded the spheres separate and a nonzero wet coefficient of restitution is observed. The critical Stokes number for the smooth SS and CS spheres is $\text{St} \approx 2.5$ and $\text{St} \approx 4$ for the roughened cases. A similar trend is seen for the alumina spheres; the smooth spheres have a critical Stokes number of $\text{St} \approx 4$, while the roughened alumina spheres have a critical Stokes number of $\text{St} \approx 5$. The difference in critical Stokes number between smooth and rough collisions is most likely due to the difference in dry coefficient of restitution. A notable feature of the plot of e versus St, for a

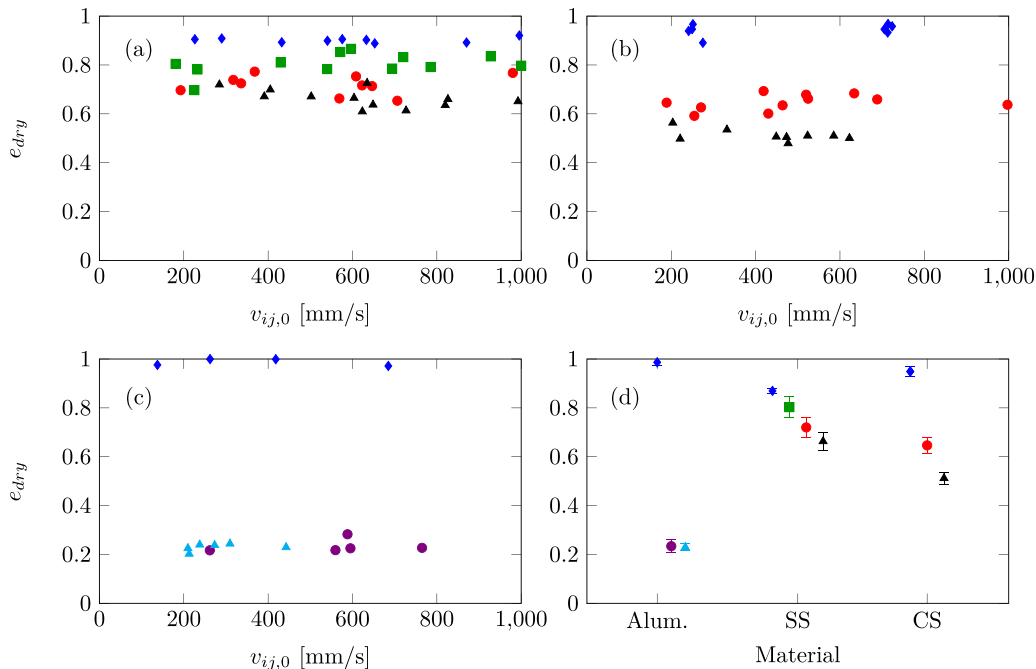


FIG. 10. A comparison of e_{dry} for a range of velocities for (a) stainless steel spheres, (b) chrome steel spheres, and (c) alumina spheres. The mean e_{dry} of all the data points for a given roughness and material is given in (d) with the error bars corresponding to the standard deviation for the data set. For a given material in (d), the roughness increases from left to right. The roughnesses considered correspond to $<1 \mu\text{m}$ (\blacklozenge), $10 \mu\text{m}$ (\blacksquare), $14 \mu\text{m}$ (\bullet), $32.5 \mu\text{m}$ (\blacktriangle), $44 \mu\text{m}$ (\blacklozenge), and $57 \mu\text{m}$ (\blacktriangle).

two-body collision, is that the gradient is steepest at the critical Stokes number and then decreases with increasing St . Previous studies have predicted that if h_{min} is constant, then the gradient will decrease with increasing h_{min} [33]. From Figs. 11(a)–11(c) it can be seen that as the roughness increases, the gradient at the critical Stokes number decreases. However, it should be noted that this lesser gradient may be an artifact of a lower dry coefficient of restitution. A lower gradient at the critical St indicates that there is more viscous dissipation. Interestingly, there is negligible difference between e versus St for the sandblasted spheres and smooth spheres in Fig. 11(d), despite the difference in dry coefficient of restitution. This idea is consistent with the idea suggested in [12,14,33] that the contact mechanism is dominated by the largest h_{min} value. For the sandblasted case, the roughness is larger than for the smooth spheres, but still smaller than h_{gt} and so the minimum separation distance derived via the glass transition pressure may still be the dominant contact mechanism.

C. Numerical simulation of rough wet collisions using DEM

Here we use DEM to simulate a moving dry sphere contacting a stationary wet sphere. These simulations are set up to mimic the parameters used to conduct the experiments. The only parameters which can be varied are either the glass transition pressure or the minimum separation distance; all other parameters are determined from the material properties of the spheres or interstitial liquid. The dry coefficient of restitution was changed for the rough and smooth cases to match the dry coefficient of restitution for each case shown in Fig. 10(d). There has been no attempt to implement a physical roughness on the particles within DEM. A coefficient of friction is also not considered. The viscous force model given in Eq. (6) is implemented in DEM and used with either the glass transition

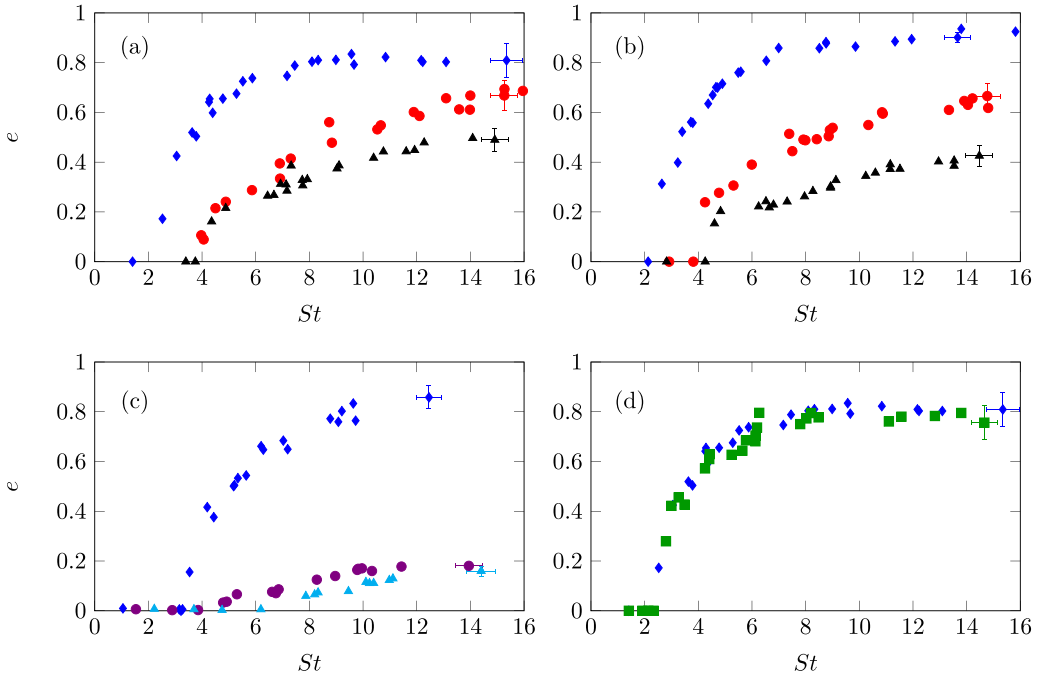


FIG. 11. Stokes number St versus the wet coefficient of restitution e for a two-body collision of (a) stainless steel, (b) chrome steel, (c) alumina, and (d) sandblasted stainless steel spheres. The markers correspond to roughnesses of $<1\ \mu\text{m}$ (\blacklozenge), $10\ \mu\text{m}$ (\bullet), $14\ \mu\text{m}$ (\blacksquare), $32.5\ \mu\text{m}$ (\blacktriangle), $45\ \mu\text{m}$ (\bullet), and $57\ \mu\text{m}$ (\blacktriangle). The SS and CS collisions are conducted using 3 Pa s silicone oil with $h_{i,j,0} = 168\ \mu\text{m}$ for the smooth collisions, $h_{i,j,0} = 200\ \mu\text{m}$ for the $14\text{-}\mu\text{m}$ roughness collisions, and $h_{i,j,0} = 220\ \mu\text{m}$ for the $32.5\text{-}\mu\text{m}$ roughness collisions. The alumina collisions are conducted using 1 Pa s silicone oil with $h_{i,j,0} = 100\ \mu\text{m}$. Chosen experiments at high St have error bars shown to provide an indication of the error in the measurements; the error bars have been removed from the other points for clarity.

minimum separation distance or the constant minimum separation distance associated with particle roughness. Figure 12 shows a comparison of the smooth and rough experimental collision data to a DEM model with the viscous force implementation using either h_{gt} or h_{Ra} .

The smooth sphere stainless steel, chrome steel, and alumina experimental data have good agreement with the viscous force model when using a minimum separation distance derived from a best-fit glass transition pressure. The glass transition model is able to capture the critical St where rebound is initiated and replicates the contact dynamics over a range of St after the critical St is reached. Further, the smooth experimental data have poor agreement when the viscous force uses a best-fit constant minimum separation distance. To obtain a match with the first nonzero e value, using the best-fit constant minimum separation distance, a value which is significantly larger than the surface roughness for the smooth spheres must be used.

For the rough sphere cases, the situation is different. As the roughness increases, the constant minimum separation distance approach provides a better match to experimental results than the glass transition approach. The DEM simulations have fair agreement with experimental data for the spheres with a roughness of $14\ \mu\text{m}$. The agreement of $14\text{-}\mu\text{m}$ roughness spheres with DEM using a glass transition approach is poorest when $St < 10$, but improves as St increases. Recall Fig. 3, where $h_{\text{gt}} \approx 10$ at $St = 10$, it is possible that the dominant mechanism to induce rebound has changed due to the increase in St . The glass transition model significantly overestimates the coefficient of restitution for spheres with a roughness of $32.5\ \mu\text{m}$. The glass transition model underestimates the viscous force which results in a value for e which is greater than measured experimentally. Both

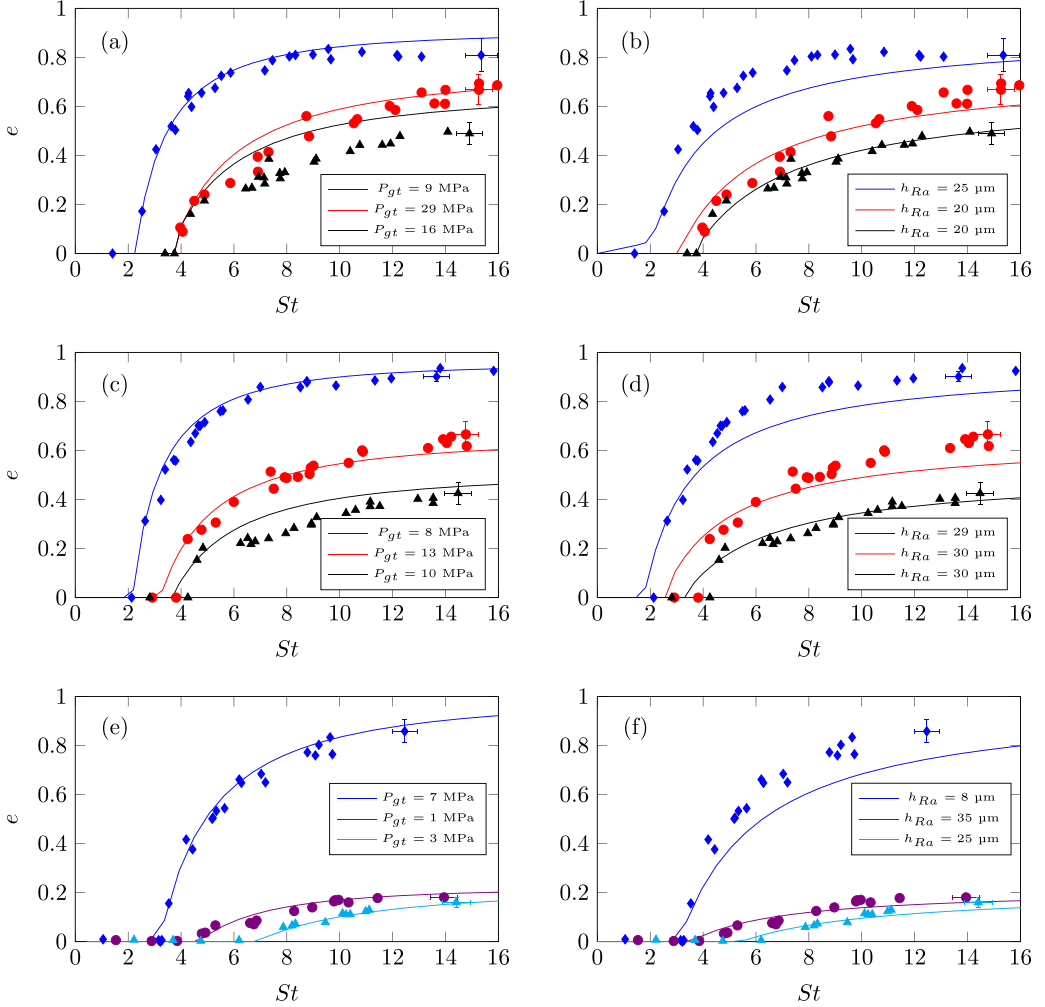


FIG. 12. Comparison of DEM viscous force model to experiments for collisions of two wetted stainless steel spheres (a), (b) chrome steel spheres (c), (d), and alumina spheres (e), (f). Experiments are given by markers and simulations by lines. The data for the metal spheres correspond to smooth spheres (\blacklozenge)(—), 14- μm roughness spheres (\bullet)(—), and 32.5- μm roughness spheres (\blacktriangle)(—). The data for the alumina spheres correspond to smooth spheres (\blacklozenge)(—), 44- μm roughness spheres (\bullet)(—), and 57- μm roughness spheres (\blacktriangle)(—). The left figures (a), (c), (e) use a minimum separation distance which is derived from the glass transition pressure [Eq. (7)], while the right figures (b), (d), (f) use a minimum separation distance which is constant.

rough alumina cases have good agreement with the DEM using the glass transition model, however, due to the minimal increase of e with increasing St , it is difficult to determine the significance of this observation. We also note that the best-fit glass transition pressure is lower for the rough alumina collisions than for the smooth alumina collisions, opposite of what is observed for the steel spheres. We attribute this difference to the complex surface of the alumina particles. Further discussions will concentrate on the steel results. The differences between smooth and rough spheres suggest that the viscous force experienced by smooth and rough spheres is not the same, and different methods of modeling the minimum separation distance should be used depending on the surface roughness of the particles. A surprising result from Fig. 12 is that for cases where the glass transition

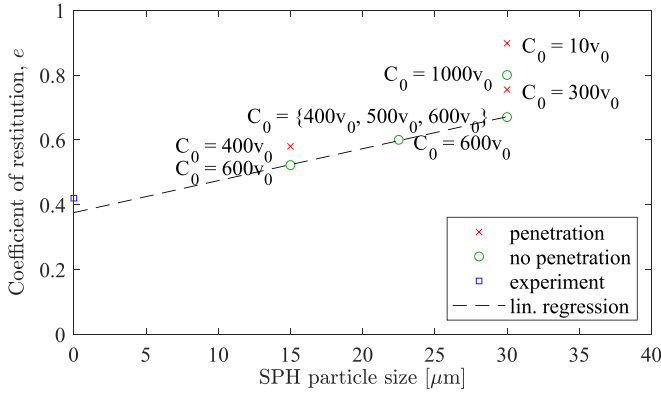


FIG. 13. The effect of SPH particle size and C_0 on the coefficient of restitution e for a smooth sphere wet particle collision.

model has poor agreement with experimental data, the constant h_{Ra} model has good agreement with experimental data and vice versa. Previous authors have suggested that the dominant mechanism for inducing rebound is dependent on whether h_{Ra} or h_{gt} is largest [12,14,33]. The results here indicate that this theory is sensible. It should be noted that the best-fit h_{min} did not vary significantly based on roughness of the particles. We hypothesize that the contact point may be dominated by the largest roughness elements, which the particle size distribution measurements in Figs. 4 and 5 show are similar for the microparticles used here, despite the difference in median particle diameter.

There is a clear difference between the wet particle contact dynamics for the smooth and rough spheres. Yet, the glass transition model does well to match experimental results for most cases. As the particle roughness increases, we require a higher glass transition pressure to match experimental data. Thus, the viscous forces are greater for the rough sphere collisions compared to the smooth sphere collisions. The increased viscous forces dissipate more kinetic energy from the rough system and the collision is less elastic than in the smooth cases. However, direct comparison between the smooth and rough particle collision data is challenging due to a number of reasons. First, the dry coefficient of restitution decreases as the particle roughness increases, which is likely due to asymmetric contacts between roughness elements [58]. Second, the film thickness is not consistent between different roughness collisions, and increases with particle roughness. Thus, we now attempt to model the smooth and rough particle collisions using smoothed particle hydrodynamics to better understand the difference in viscous force for smooth and rough particles.

D. SPH simulation of wet particle collisions

Smoothed particle hydrodynamics (SPH) is used to investigate the fluid flow between two spheres during a collision. First, we consider a case where the surface of the spheres is smooth. The smooth sphere SPH simulation uses the same conditions for one particular setting investigated experimentally for smooth stainless steel collisions.

The maximum flow velocity in the fluid domain was initially unknown. Therefore, the artificial speed of sound C_0 was initially set to $C_0 = 10v_{ij,0}$. However, the low artificial speed of sound and, consequently, smaller pressure reaction of the fluid in the contact area did not prevent the liquid SPH particles from penetrating the boundary particles. This resulted in no viscous slowing down of the DEM spheres, and the coefficient of restitution was the same as for the dry case. As a consequence of this nonphysical behavior, the artificial speed of sound was increased until no penetration occurs. Figure 13 shows the effect of C_0 and SPH particle size on e for a smooth particle collision.

As the SPH liquid particle size is decreased, the coefficient of restitution resolved from the SPH simulations approaches the coefficient of restitution resolved experimentally. However, as the liquid

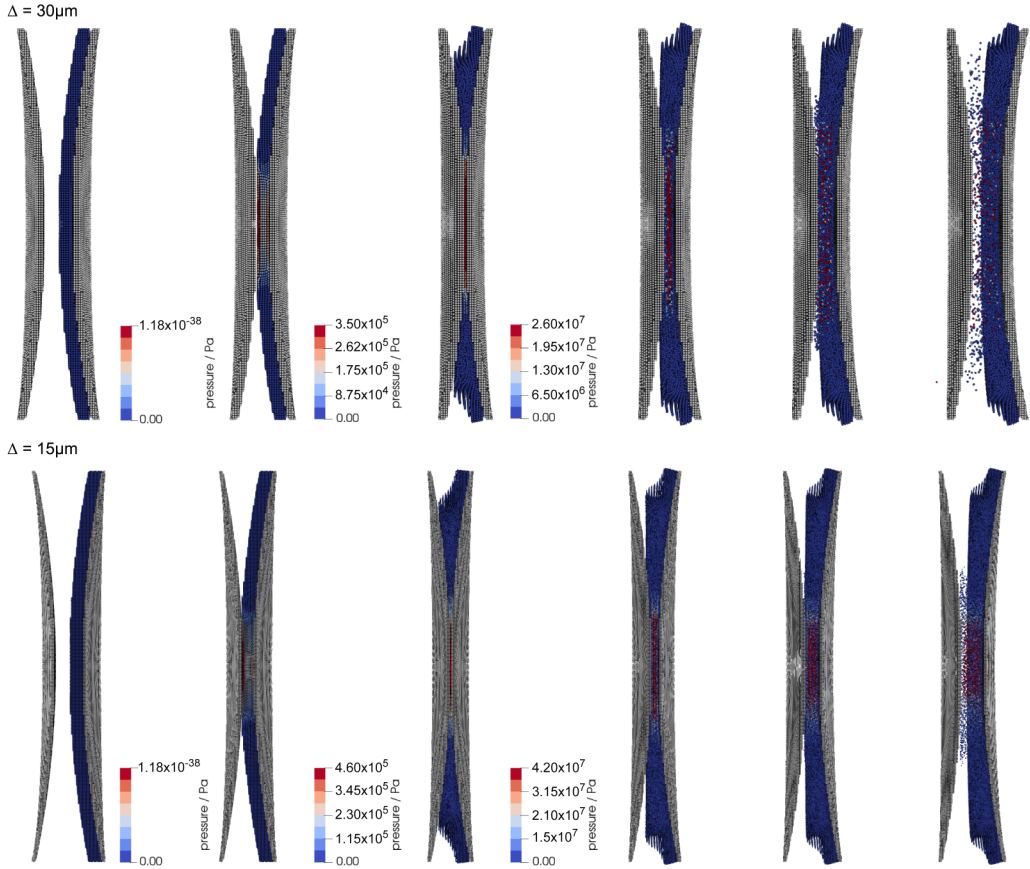


FIG. 14. Pressure distribution for a collision of smooth wetted spheres at $v_{ij,0} = 0.205 \text{ m s}^{-1}$, artificial speed of sound $C_0 = 600v_{ij,0}$, and SPH particle sizes of $\Delta = 30 \mu\text{m}$ (top) and $\Delta = 15 \mu\text{m}$ (bottom). Collision progresses from left to right, and the same time points are presented for both simulations. The SPH boundary particles are colored gray, while the DEM spheres are not shown for clarity.

SPH particle size is decreased, the artificial speed of sound must be increased to ensure the liquid SPH particles do not penetrate the boundary particles. Above some minimum C_0 , further slight change in the artificial speed of sound had negligible effect on the coefficient of restitution. However, when C_0 was significantly larger than the minimum artificial speed of sound required to stop particle penetration, the coefficient of restitution increased. This can be attributed to the increasing stiffness of the liquid phase, which allows less dissipation during the collision. Linear regression performed on the coefficient of restitution for the SPH simulations suggests that as the liquid SPH particle size approaches zero, the coefficient of restitution will approach $e = 0.39$. This value of e is similar to our experimentally measured value of $e = 0.41$. Thus, SPH can be used to capture the viscous slowing down effects caused in pendular regime particle collisions for smooth particles.

Figure 14 shows the pressure distribution and the fluid flow during the collision for two different SPH particles sizes, 30 and 15 μm . Here, both SPH simulations have an artificial speed of sound of $C_0 = 600v_{ij,0}$.

As the striking sphere penetrates the liquid layer of the stationary sphere, the liquid is displaced to the sides, and the fluid pressure in the contact region rises. As penetration continues, the fluid is further compressed until the separation between spheres is one SPH particle diameter while the DEM spheres come in contact. After the solid-solid contact, as the spheres begin to separate, the

growing void in the contact region fills with fluid represented by SPH particles. This is similar to what is observed experimentally, where the liquid fills the void between separating spheres and a liquid bridge is elongated between the two separating spheres. However, in the SPH simulations, many liquid SPH particles also have a high pressure in this liquid bridge region, and the pressure is inconsistent across the radius of the bridge. It is expected that the highest pressure will be through the central axis of the bridge, yet the pressure distribution throughout the liquid SPH particles appears dependent on the pre-separation position of each liquid SPH particle. Consequently, the SPH model for smooth wetted spheres shows good agreement with the experimental results during the impact phase and estimation of the coefficient of restitution. However, it requires further improvement for the analysis of postcollision phenomena.

Figure 14 shows that the pressure in the interstitial liquid region increases as the SPH particle size decreases. The maximum pressure in the SPH simulations is $P \approx 4 \times 10^7$ Pa (40 MPa) for an SPH particle size of $\Delta = 15$ μm . This is significantly less than the glass transition pressure of silicone oil ($P_{gt} = 400$ MPa) [68], but significantly more than the glass transition pressure used to match experimental results for the DEM simulations ($P_{gt} = 9$ MPa) in Fig. 12. Previous authors have found that the Davis viscous force model [Eq. (6)] slightly over predicts the viscous force between two spheres [28]. The SPH results indicate a higher pressure is reached in the interstitial liquid than what is used as the minimum glass transition pressure for the DEM simulations, which corroborates the idea that the viscous forces are being overestimated.

The SPH method is now extended onto rough spheres. First we simulate a stainless steel sphere with a roughness of 32.5 μm . These simulations are analogous to the experiments conducted earlier in this study for which stainless steel spheres were coated with 65- μm diameter microspheres to induce a roughness. A single experimental case is considered, for which the initial conditions are $v_{ij,0} = 0.288$ m s^{-1} , $h_{ij,0} = 220$ μm , $e_{dry} = 0.66$. These initial conditions are implemented in SPH in an attempt to replicate the experimentally measured wet coefficient of restitution $e = 0.161$. The SEM images of the rough sphere surfaces used in the experiments show that the microspheres are randomly distributed (see Fig. 5). Thus, the roughness modeling is simplified as presented earlier in Fig. 9 (Sec. III D). Here we consider two alignments of roughness elements for the contacting spheres: (1) the roughness elements are aligned such that the zenith of a hemispherical roughness element will contact the zenith of another hemispherical roughness element, and (2) an alignment such that the contacting roughness hemisphere will contact in the trough between two hemispherical roughness elements on the stationary sphere. These alignments are referred to as a central collision (i.e. contact at the zenith of roughness elements), and an interlocking collision (i.e. contact at the trough between roughness elements). Real world collisions between wetted particles will likely be somewhere between an interlocking collision and a central collision. Figure 15 shows how the wet coefficient of restitution changes for a 32.5- μm roughness collision as this alignment changes and the SPH particle size is decreased.

The interlocking collision has a lower e than the central collision. As the roughness elements interlock, there is a smaller volume for the fluid to occupy and so the pressure is higher. The increase in pressure results in more viscous dissipation and so the coefficient of restitution is lower. However, the slight difference between the two methods indicates that this is likely of negligible importance to consider in the future. Interesting to note is that decreasing the SPH particle size does not decrease the coefficient of restitution for the rough collisions. This may be due to the fluid phase being well resolved at higher SPH particle sizes; however, a more likely explanation is that the flow through fine channels between roughness elements is limited due to a relatively large SPH particle size. SPH simulations using SPH particle sizes $\Delta < 15$ μm were unable to be investigated due to the high wall-clock time required.

Figure 16 shows the evolution of the fluid pressure during the collision for stainless steel spheres with a roughness of 32.5 μm . The collision is presented using a 2D view, for ease of visualizing the pressure distribution, and thus the roughness elements look slightly different than in Fig. 9.

As the striking sphere contacts the liquid film, the interstitial liquid is squeezed and increases in pressure. It can be seen that the pressure increase is high near the zenith of roughness elements, but

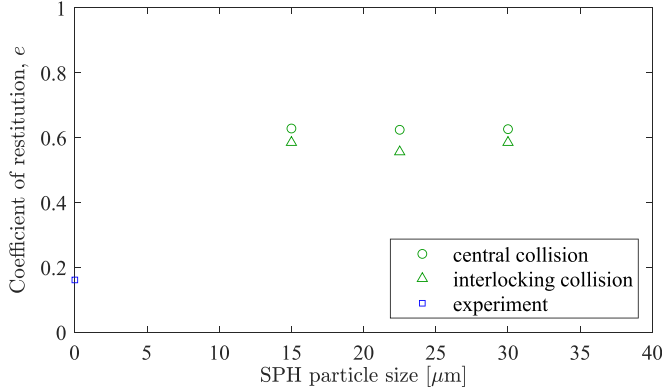


FIG. 15. The effect of SPH particle size on the coefficient of restitution e for a 32.5- μm roughness sphere wet particle collision. The initial conditions are $v_{ij,0} = 0.288 \text{ m s}^{-1}$, $h_{i,j,0} = 220 \mu\text{m}$, and $e_{\text{dry}} = 0.66$.

remains low in the troughs between roughness elements. The pressure also increases faster for the striking sphere than the stationary sphere. A pressure gradient between the two spheres develops with its minimum in the gaps between the roughness spheres, thus causing a secondary flow into the gaps. This additional flow reduces the viscous dissipation on the striking particle and results in a higher coefficient of restitution. The pressure gradient from the contacting roughness elements radiates outwards towards the outer of the liquid film, with the maximum pressure at the center of the contacting roughness elements. The pressure gradient is coincident with the primary flow of the displaced liquid to the outer region. During the separation of the spheres, i.e., stretching of the liquid bridge, the pressure decreases in the contact zone with increasing distance of the two spheres. The displaced fluid, on the other hand, remains outside of the contact zone.

The pressure for the SPH simulations of the rough spheres is $P \approx 2 \times 10^7 \text{ Pa}$ (20 MPa) for the central collision, and $P \approx 5 \times 10^7 \text{ Pa}$ (50 MPa) for the interlocking collision, both for an SPH particle size of $\Delta = 15 \mu\text{m}$. The pressure difference between the two setups can be explained by the higher compression of the liquid by the interlocking roughness spheres until the roughness spheres create a solid-solid contact, while for the central collision the fluid in the gaps between the roughness spheres is not compressed as much as the spheres create a solid-solid contact earlier.

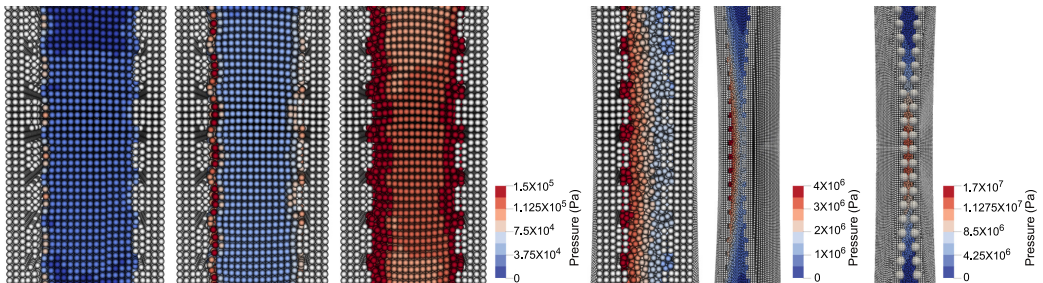


FIG. 16. Pressure distribution for a collision of 32.5- μm roughness wetted spheres at $v_{ij,0} = 0.288 \text{ m s}^{-1}$, artificial speed of sound $C_0 = 600v_{ij,0}$, and SPH particle sizes of $\Delta = 15 \mu\text{m}$. Collision progresses from left to right. The SPH boundary particles are colored gray, while the DEM spheres are not shown for clarity. Left: the pressure evolution at the start of the contact on the initial contact of dry sphere onto the wetted sphere is shown. Middle: the pressure gradient between the two spheres, and from the contact zone to the outer region at a later time point before the solid contact occurs, can be seen. Right: the pressure gradient during the solid contact point of the surface roughness, which are visualized here for clarity in contrast to the other images.

Surprisingly, this large difference in maximum pressure causes a very small difference in coefficient of restitution. This indicates that it is entirely plausible that the interstitial liquid reaches pressures which can induce a glass transition, even for relatively low velocities. Of further interest is that the maximum pressures for rough collisions are similar to those observed in SPH simulations for smooth spheres, $P \approx 42$ MPa for $\Delta = 15$ μm and $P \approx 26$ MPa for $\Delta = 30$ μm . Yet, for the smooth case the increase in maximum pressure correlates to a large decrease in coefficient of restitution.

The SPH simulation results give new insight into the fluid pressure and fluid flow during the collision of smooth and rough wetted spheres. For smooth spheres, the experimentally measured coefficient of restitution can be accurately predicted by SPH as the SPH particle size decreases, and the maximum pressure was found to be significantly larger than the pressure associated with a best-fit minimum separation distance based on the glass transition pressure. The difference in pressure between the DEM and SPH simulations suggests that the viscous force model implemented in DEM overestimates the viscous force and thus must use a lower glass transition pressure to compensate. For the rough spheres, the SPH method can not accurately predict the experimentally measured coefficient of restitution. The reason for this divergent behavior still needs to be clarified and more work should be conducted on this topic in the future. Nonetheless, the rough SPH simulations showed that the fluid can flow through microchannels between roughness elements to dissipate pressure which reduces the viscous slowing of the striking particle and increases the coefficient of restitution. This phenomenon is expected to still be present for more accurate rough SPH simulations.

V. CONCLUSION

In this work we investigated rectilinear collisions between wetted spheres of varying surface roughness. As the surface roughness of the spheres increased, more kinetic energy was dissipated from the system and the coefficient of restitution decreased. The Davis viscous force model was compared to smooth and rough experiments to verify the hypothesis that the contact is dependent on the longer length scale associated with either the roughness or the glass transition pressure. DEM simulations which use the glass transition length scale had the best agreement with experimental wet collisions of particles with a roughness smaller than the length scale associated with the glass transition pressure. Comparatively, DEM simulations which use a constant minimum separation distance had the best agreement with experimental wet collisions of particles with a roughness which exceeded the length scale associated with the glass transition pressure. Thus, we strongly suggest that the Davis viscous force model be used when the roughness of the particles is less than the length scale associated with the glass transition pressure and vice versa. Many real systems will have a roughness which is greater than the glass transition length, and so we expect that a constant h_{min} model is likely to be the most suitable model. However, this needs to be explored further for many particulate systems.

Select collisions were also modeled using SPH. The SPH method was found to accurately model smooth sphere collisions, if the SPH particle size was small enough. Furthermore, the maximum SPH pressure was larger than the best-fit glass transition pressure, which suggests that the Davis viscous force equation overestimates the viscous forces. Although the rough SPH simulations could not accurately predict the experimentally measured coefficient of restitution, SPH was able to show that the penetrating sphere displaces the interstitial liquid on impact, causing higher pressure near the striking sphere, and creating flow into low pressure regions between roughness elements. The flow in-between roughness elements is hypothesized to be critical to reducing the viscous force experienced by particles.

ACKNOWLEDGMENTS

Parts of this research were done while P. Eberhard visited the University of Canterbury, New Zealand, supported by an Erskine Fellowship and while A. Baumann visited supported

by the SPP 1897 funded by the German Research Foundation. All this support is highly appreciated.

-
- [1] Z. Lai, Y. Xia, and Q. Chen, Discrete element modeling of granular hopper flow of irregular-shaped deformable particles, *Adv. Powder Technol.* **34**, 104106 (2023).
 - [2] L. Sheng, W. Chang, and S. Hsiau, Influence of particle surface roughness on creeping granular motion, *Phys. Rev. E* **94**, 012903 (2016).
 - [3] I. Goldhirsch, Rapid granular flows, *Annu. Rev. Fluid Mech.* **35**, 267 (2003).
 - [4] K. Kamrin, Non-locality in granular flow: Phenomenology and modeling approaches, *Front. Phys.* **7**, 1 (2019).
 - [5] M. Danczyk, T. Meaclem, M. Mehdizad, D. Clarke, P. Galvosas, L. Fullard, and D. Holland, Influence of contact parameters on discrete element method (DEM) simulations of flow from a hopper: Comparison with magnetic resonance imaging (MRI) measurements, *Powder Technol.* **372**, 671 (2020).
 - [6] C. R. K. Windows-Yule, D. R. Tunuguntla, and D. J. Parker, Numerical modelling of granular flows: A reality check, *Comput. Part. Mech.* **3**, 311 (2016).
 - [7] T. Pähitz, O. Durán, D. N. de Klerk, I. Govender, and M. Trulsson, Local rheology relation with variable yield stress ratio across dry, wet, dense, and dilute granular flows, *Phys. Rev. Lett.* **123**, 048001 (2019).
 - [8] S. Schmelzle and N. Herrmann, DEM simulations: Mixing of dry and wet granular material with different contact angles, *Granul. Matter.* **20**, 19 (2018).
 - [9] T. Tang, Y. He, A. Ren, and T. Wang, Experimental study and dem numerical simulation of dry/wet particle flow behaviors in a spouted bed, *Ind. Eng. Chem. Res.* **58**, 15353 (2019).
 - [10] G. Gagneux, O. Millet, B. Mielniczuk, and M. S. El Youssefi, Theoretical and experimental study of pendular regime in unsaturated granular media, *Eur. J. Environ. Civ. Eng.* **21**, 840 (2017).
 - [11] T. T. Vo, S. Nezamabadi, P. Mutabaruka, J.-Y. Delenne, and F. Radjai, Additive rheology of complex granular flows, *Nat. Commun.* **11**, 1476 (2020).
 - [12] R. H. Davis, J. W. Sition, Oblique collisions of two wetted spheres, *Phys. Rev. Fluids* **5**, 054305 (2020).
 - [13] K. Washino, E. L. Chan, T. Matsumoto, S. Hashino, T. Tsuji, and T. Tanaka, Normal viscous force of pendular liquid bridge between two relatively moving particles, *J. Colloid Interface Sci.* **494**, 255 (2017).
 - [14] C. M. Donahue, C. M. Hrenya, R. H. Davis, K. J. Nakagawa, A. P. Zelinskaya, and G. G. Joseph, Stokes' cradle: normal three-body collisions between wetted particles, *J. Fluid Mech.* **650**, 479 (2010).
 - [15] C. S. Campbell, Granular material flows-An overview, *Powder Technol.* **162**, 208 (2006).
 - [16] C. Goujon, N. Thomas, and B. Dalloz-Dubrujeaud, Monodisperse dry granular flows on inclined planes: Role of roughness, *Eur. Phys. J. E* **11**, 147 (2003).
 - [17] O. Pouliquen, Scaling laws in granular flows down rough inclined planes, *Phys. Fluids* **11**, 542 (1999).
 - [18] Y. C. Zhou, B. H. Xu, A. B. Yu, and P. Zulli, Numerical investigation of the angle of repose of monosized spheres, *Phys. Rev. E* **64**, 021301 (2001).
 - [19] O. Punch, M. Danczyk, M. Hawken, and D. J. Holland, A comparison of pendulum experiments and discrete-element simulations of oblique collisions of wet spheres, *AIChE J.* **69**, e17989 (2023).
 - [20] R. G. Cain, N. W. Page, and S. Biggs, Microscopic and macroscopic effects of surface lubricant films in granular shear, *Phys. Rev. E* **62**, 8369 (2000).
 - [21] B. Buck and S. Heinrich, Collision dynamics of wet particles: Comparison of literature models to new experiments, *Adv. Powder Technol.* **30**, 3241 (2019).
 - [22] B. Buck, Y. Tang, S. Heinrich, N. G. Deen, and J. A. M. Kuipers, Collision dynamics of wet solids: Rebound and rotation, *Powder Technol.* **316**, 218 (2017).
 - [23] S. Antonyuk, S. Heinrich, N. Deen, and H. Kuipers, Influence of liquid layers on energy absorption during particle impact, *Particuology* **7**, 245 (2009).

- [24] V. Sutkar, N. Deen, J. Padding, V. Salikov, B. Buck, S. Antonyuk, S. Heinrich, and H. Kuipers, A novel approach to determine wet restitution coefficients through a unified correlation and energy analysis, *AIChE J.* **61**, 769 (2015).
- [25] R. H. Davis, D. A. Rager, and B. T. Good, Elastohydrodynamic rebound of spheres from coated surfaces, *J. Fluid Mech.* **468**, 107 (2002).
- [26] F. L. Yang and M. L. Hunt, Dynamics of particle-particle collisions in a viscous liquid, *Phys. Fluids* **18**, 121506 (2006).
- [27] M. Danczyk, O. Punch, L. Fullard, M. Hawken, and D. J. Holland, A comparison of models of linear collisions between spherical particles in the pendular regime, *Powder Technol.* **398**, 117112 (2022).
- [28] O. Punch, A. Heenan, A. Marshall, and D. J. Holland, Characterization of the contact dynamics of spheres coated in a thin viscous film using an electrified Newton's cradle, *AIChE J.* **70**, e18309 (2024).
- [29] G. G. Joseph, and M. L. Hunt, Oblique particle-wall collisions in a liquid, *J. Fluid Mech.* **510**, 71 (2004).
- [30] G. G. Joseph, R. Zenit, and M. L. Hunt, Particle-wall collisions in a viscous fluid, *J. Fluid Mech.* **433**, 329 (2001).
- [31] P. Gondret, M. Lance, and L. Petit, Bouncing motion of spherical particles in fluids, *Phys. Fluids* **14**, 643 (2002).
- [32] P. Gondret, E. Hallouin, M. Lance, and L. Petit, Experiments on the motion of a solid sphere toward a wall: From viscous dissipation to elastohydrodynamic bouncing, *Phys. Fluids* **11**, 2803 (1999).
- [33] R. H. Davis, Simultaneous and sequential collisions of three wetted spheres, *J. Fluid Mech.* **881**, 983 (2019).
- [34] G. Barnocky and R. H. Davis, Elastohydrodynamic collision and rebound of spheres: Experimental verification, *Phys. Fluids* **31**, 1324 (1988).
- [35] F. Krull, J. Mathy, P. Breuninger, and S. Antonyuk, Influence of the surface roughness on the collision behavior of fine particles in ambient fluids, *Powder Technol.* **392**, 58 (2021).
- [36] O. Reynolds, On the theory of lubrication and its application to Mr. Beauchamp Tower's experiments, including an experimental determination of the viscosity of olive oil, *Philos. Trans. R. Soc.* **177**, 157 (1886).
- [37] S. T. Nase, W. L. Vargas, A. A. Abatan, and J. J. McCarthy, Discrete characterization tools for cohesive granular material, *Powder Technol.* **116**, 214 (2001).
- [38] P. Liu, R. Yang, and A. Yu, DEM study of the transverse mixing of wet particles in rotating drums, *Chem. Eng. Sci.* **86**, 99 (2013).
- [39] L. A. Easo, Liquid dispersion in sheared particulate material, Ph.D. thesis, Purdue University, 2017.
- [40] J. Horabik and M. Molenda, Parameters and contact models for DEM simulations of agricultural granular materials: A review, *Biosyst. Eng.* **147**, 206 (2016).
- [41] G. Barnocky and R. H. Davis, The influence of pressure-dependent density and viscosity on the elastohydrodynamic collision and rebound of two spheres, *J. Fluid Mech.* **209**, 501 (1989).
- [42] A. A. Kantak and R. H. Davis, Elastohydrodynamic theory for wet oblique collisions, *Powder Technol.* **168**, 42 (2006).
- [43] J. J. Monaghan, Smoothed particle hydrodynamics, *Annu. Rev. Astron. Astrophys.* **30**, 543 (1992).
- [44] L. B. Lucy, A numerical approach to the testing of the fission hypothesis, *Astrophys. J.* **82**, 1013 (1977).
- [45] A. Baumann, E. Oezkaya, D. Schnabel, D. Biermann, and P. Eberhard, Cutting-fluid flow with chip evacuation during deep-hole drilling with twist drills, *Eur. J. Mech. B Fluids* **89**, 473 (2021).
- [46] M. Robinson, M. Ramaioli, and S. Luding, Fluid-particle flow simulations using two-way-coupled mesoscale SPH-DEM and validation, *Int. J. Multiphase Flow* **59**, 121 (2014).
- [47] G. Wang, A. Riaz, and B. Balachandran, Smooth particle hydrodynamics studies of wet granular column collapses, *Acta Geotech.* **15**, 1205 (2020).
- [48] C. Kloss, C. Goniva, A. Hager, S. Amberger, and S. Pirker, Models, algorithms and validation for opensource DEM and CFD-DEM, *Prog. Comput. Fluid Dyn.* **12**, 140 (2012).
- [49] R. H. Davis, J. M. Serayssol, and E. J. Hinch, The elastohydrodynamic collision of two spheres, *J. Fluid Mech.* **163**, 479 (1986).
- [50] M. B. Liu and G. R. Liu, Smoothed particle hydrodynamics (SPH): An overview and recent developments, *Arch. Comput. Methods Eng.* **17**, 25 (2010).

- [51] D. Violeau and B. D. Rogers, Smoothed particle hydrodynamics (SPH) for free-surface flows: past, present and future, *J. Hydraul. Res.* **54**, 1 (2016).
- [52] M. S. Shadloo and M. Yildiz, Numerical modeling of Kelvin-Helmholtz instability using smoothed particle hydrodynamics, *Numer. Methods Eng.* **87**, 988 (2011).
- [53] D. McLean, *Understanding Aerodynamics: Arguing from the Real Physics* (Wiley, Hoboken, NJ, 2012).
- [54] R. H. Cole, *Underwater Explosions* (Dover, New York, 1948).
- [55] J. J. Monaghan, Simulating free surface flows with SPH, *J. Comput. Phys.* **110**, 399 (1994).
- [56] L. Fries, S. Antonyuk, S. Heinrich, D. Dopfer, and S. Palzer, Collision dynamics in fluidised bed granulators: A DEM-CFD study, *Chem. Eng. Sci.* **86**, 108 (2013).
- [57] P. Holoborodko, Smooth Noise Robust Differentiators (2008), <http://www.holoborodko.com/pavel/numerical-methods/numerical-derivative/smooth-low-noise-differentiators>.
- [58] X. Li, M. Dong, D. Jiang, S. Li, and Y. Shang, The effect of surface roughness on normal restitution coefficient, adhesion force and friction coefficient of the particle-wall collision, *Powder Technol.* **362**, 17 (2020).
- [59] Q. Fu and W. Sun, Mie theory for light scattering by a spherical particle in an absorbing medium, *Appl. Opt.* **40**, 1354 (2001).
- [60] N. Otsu, A threshold selection method from gray-level histograms, *IEEE Trans. Syst. Man Cybern. Syst.* **9**, 62 (1979).
- [61] W. C. Swope, H. C. Andersen, P. H. Berens, and K. R. Wilson, A computer simulation method for the calculation of equilibrium constants for the formation of physical clusters of molecules: Application to small water clusters, *Chem. Phys.* **76**, 637 (1982).
- [62] F. Fleissner, *Parallel Object Oriented Simulation with Lagrangian Particle Methods* (Shaker, Herzogenrath, 2010).
- [63] S. Adami, X. Hu, and N. Adams, A generalized wall boundary condition for smoothed particle hydrodynamics, *J. Comput. Phys.* **231**, 7057 (2012).
- [64] G. Kuwabara and K. Kono, Restitution coefficient in a collision between two spheres, *Jpn. J. Appl. Phys.* **26**, 1230 (1987).
- [65] J. Bonet and T.-S. L. Lok, Variational and momentum preservation aspects of smooth particle hydrodynamic formulations, *Comput. Methods Appl. Mech. Eng.* **180**, 97 (1999).
- [66] D. Molteni and A. Colagrossi, A simple procedure to improve the pressure evaluation in hydrodynamic context using the SPH, *Comput. Phys. Commun.* **180**, 861 (2009).
- [67] M. C. Marinack, R. E. Musgrave, and C. F. Higgs, Experimental investigations on the coefficient of restitution of single particles, *Tribol. Trans.* **56**, 572 (2013).
- [68] S. Bair, The viscosity at the glass transition of a liquid lubricant, *Friction* **7**, 86 (2019).